Computers and Mathematics with Applications 58 (2009) 940–949

Contents lists available at ScienceDirect

Computers and Mathematics with Applications

journal homepage: www.elsevier.com/locate/camwa

Boundary conditions for lattice Boltzmann simulations with complex geometry flows

Cheng Chang, Chih-Hao Liu, Chao-An Lin *

Department of Power Mechanical Engineering, National Tsing Hua University, Hsinchu 300, Taiwan

ARTICLE INFO

Keywords:
Boundary conditions
Lattice Boltzmann method
Complex geometry
Unsteady flow

ABSTRACT

Boundary conditions of lattice Boltzmann method to simulate flows embedded with a solid object is proposed. The closest nodes adjacent to the boundary in the fluid domain are used as boundary nodes of the flow domain. The fluid velocity of the boundary node is obtained by linear interpolation between the velocities of the solid object and the second fluid node further away. Then, distribution functions originating from the solid domain at the boundary nodes are modified using known distribution functions and correctors to satisfy the momentum. This boundary condition is an extended form of a method proposed by Hou et al. [C.F. Hou, C. Chang, C.A. Lin, Consistent boundary conditions for 2D and 3D Lattice Boltzmann simulations (submitted for publication)] for plane wall and regular geometry. The technique is examined by simulating decaying vortex, transient flow induced by an abruptly rotating ring and flow over an asymmetrically placed cylinder. Numerical simulations indicate that this method is second order accurate, and all the numerical results are compatible with the benchmark solutions.

1. Introduction

The Lattice Boltzmann method (LBM) [1–3] has been successfully applied to various hydrodynamic problems and the major advantages of the LBM are explicit, easy to implement, and natural to parallelize. However, the capability of the lattice Boltzmann method to model complex geometry may not be trivial due to the Cartesian grid adopted and the complex boundary implementation along the curved boundary. The difficulties encountered are two folds. Firstly the representation of the complex geometry, since the Cartesian grid does not conform with the curved boundary. Secondly the correct implementation of the boundary conditions, where incorrect distribution functions originated from the solid nodes external to the flow domain are encountered during the streaming operation.

Various methodologies have been put forward to tackle the LBM simulation of complex geometry flows. For example, Chen et al. [4] extended the "extrapolation scheme" to curved boundary, where the boundary is represented by the lattice nodes closest to the curved surface using castellated approach. The adjacent nodes whose distribution functions streaming to the castellated boundary nodes are inside the solid domain, and the distribution functions at these solid nodes are calculated using a second order extrapolation. Filippova and Hanel [5] proposed a method using a simple linear interpolation between a fictitious equilibrium distribution function and a well-chosen near-boundary distribution function. The weighting factor of the interpolation is determined by the distance between the boundary and the near-boundary lattice. Mei et al. [6] further improved its numerical stability. Lallemand and Luo [7] combined the bounce-back scheme and interpolation scheme to treat a moving curved boundary by the lattice Boltzmann method. The bounce-back scheme simulates a stationary boundary, and an additional term is added to implement a moving boundary. This treatment is an extension of that proposed by Bouzidi

* Corresponding author.
E-mail address: calin@pme.nthu.edu.tw (C.-A. Lin).

0898-1221/$ – see front matter © 2009 Elsevier Ltd. All rights reserved.
doi:10.1016/j.camwa.2009.02.016

et al. [8]. One point boundary condition was proposed by Junk and Yang [9], where a correction to the bounce back boundary condition improves the accuracy of pressure and velocity.

Alternatively, the immersed boundary method (IBM) is another convenient approach to treat fluid flows involving complex boundary, though it was formulated mostly within the Navier-Stkes equation framework. The complex geometry within the Cartesian grid can be simulated by generating external force field to mimic the immersed boundary. IBM can be categorized as feedback forcing [10,11] and direct forcing [12] approaches. However, the major drawback of the existing feedback forcing is the restriction of small CFL number. Aiming at improving the CFL number restriction, Su et al. [13] proposed a new immersed boundary (IB) technique for the simulation of flows interacting with solid boundary within the Navier–Stokes framework. In Chen et al. [14], the lattice Boltzmann method is combined with the immersed boundary technique of Su et al. [13] to simulate flows with complex boundary. In Su et al. and Chen et al., dirac delta function was employed to link the force between the Lagrangian marker and the computational grid, and this may potentially smear the solution across the interface.

In the present study, a novel technique is proposed to model the solid object embedded with the flow domain and it does not involve force as contrasted to the work of Chen et al. [14]. Here, the curved boundary is represented by a series of Lagrangian markers. The fluid velocity of node adjacent to the solid boundary is obtained by linear interpolation between the Lagrangian marker and the second fluid node further away. Then distribution functions originates from the solid domain at the nodes adjacent to the solid curved boundary are modified using known distribution functions and correctors, where the correctors at these nodes are obtained directly from the definitions of density and momentum. This curved boundary technique is an extended form of a method proposed by Hou et al. [15] for plane wall and regular geometry. The validity and the accuracy of the new method are scrutinized by simulating decaying vortex flow, transient flow induced by an abruptly rotating ring and flow over an asymmetrically placed cylinder.

2. The lattice Boltzmann method

2.1. The lattice Boltzmann equation

The lattice Boltzmann equation adopting a uniform lattice with Bhatnagar–Gross–Krook collision model [1–3] can be expressed as,

$$f_i^+(\vec{x}, t) = f_i(\vec{x}, t) - \frac{1}{\tau}[f_i(\vec{x}, t) - f_i^{eq}(\vec{x}, t)] \tag{1}$$

$$f_i(\vec{x} + \vec{e}_i \mathrm{d}t, t + \mathrm{d}t) = f_i^+(\vec{x}, t) \tag{2}$$

where f_i is the particle distribution function along the particle speed direction $\vec{e}_i$ at position $\vec{x}$ and time t. f_i^{eq} is the equilibrium distribution function and τ is the single relaxation time that controls the rate approaching equilibrium. The above two equations represent collision and streaming operations, respectively.

Based on the particle distribution function, the macroscopic density ρ and velocity $\vec{u}$ are defined as,

$$\sum_i f_i = \rho, \qquad \sum_i f_i \vec{e}_i = \rho \vec{u}. \tag{3}$$

The equilibrium distribution functions, which depend on the local density and velocity, are given by the form [2],

$$f_i^{eq} = \omega_i \rho \left[1 + \frac{3}{c^2}\vec{e}_i \cdot \vec{u} + \frac{9}{2c^4}(\vec{e}_i \cdot \vec{u})^2 - \frac{3}{2c^2}\vec{u} \cdot \vec{u}\right] \tag{4}$$

where $c = \mathrm{d}x/\mathrm{d}t$ is the lattice speed, and $\mathrm{d}x$ and $\mathrm{d}t$ are the lattice width and time step, respectively. Here, $\mathrm{d}t$ is chosen to be equal to $\mathrm{d}x$, thus $c = 1$. ω_i is a weighting factor. For the present 2D applications, D2Q9 model are adopted (see Fig. 1). The particle speed $\vec{e}_i$ adopting D2Q9 model are defined as,

$$\vec{e}_0 = 0 \tag{5}$$

$$\vec{e}_i = (\cos[\pi(i-1)/2], \sin[\pi(i-1)/2])c \quad i = 1, 2, 3, 4 \tag{6}$$

$$\vec{e}_i = (\cos[\pi(i-4-1/2)/2], \sin[\pi(i-4-1/2)/2])\sqrt{2}c \quad i = 5, 6, 7, 8 \tag{7}$$

and the weighting factors are $\omega_0 = 4/9$, $\omega_{i=1,2,3,4} = 1/9$, and $\omega_{i=5,6,7,8} = 1/36$. Moreover, the speed of sound is $C_s = c/\sqrt{3}$ and the corresponding kinematic viscosity is $\nu = (\tau - 0.5)C_s^2 \mathrm{d}t$ in the simulation.

3. Boundary conditions

A typical computational domain with a solid object embedded within is shown in Fig. 2. In the present approach, LBM simulation is applied throughout the computational domain, i.e. even within the solid. Therefore, two different boundary conditions have to be addressed. The first one is the boundary condition along the computational domain (thick solid line), and the second one is how to represent the solid–fluid boundary. Here, the derivation of the boundary condition is based on the known or assumed velocity (u, v) distributions along these boundaries.

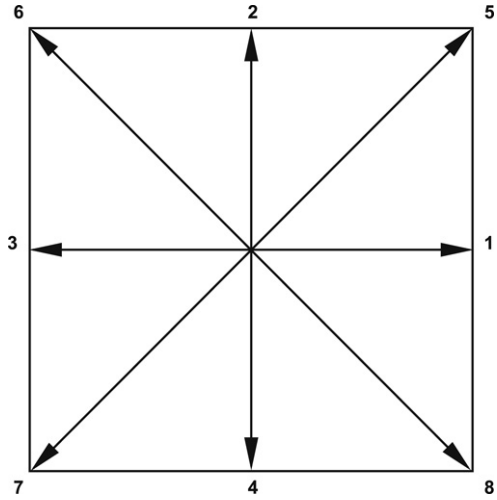

Fig. 1. d2q9 model.

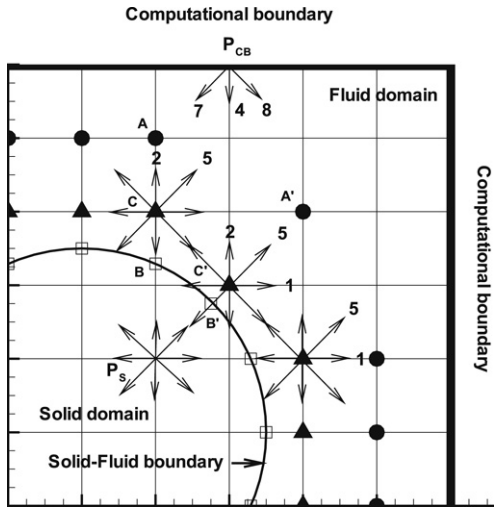

Fig. 2. Distribution functions along the boundary nodes. ▲: correction node, □: Lagrangian marker, ●: second fluid node.

3.1. Computational domain

Along the computational boundary, $f_i(\vec{x}, t)$ due to the inward streaming operations may originate from the undefined nodes external to the computational domain, therefore measures have to be taken to prescribe these unknown particle distribution functions, which are denoted as $f_{i=p}(\vec{x}, t)$. Obviously, $f_{i\neq p}(\vec{x}, t) = f^{+}_{i\neq p}(\vec{x} - \vec{e}_i \mathrm{d}t, t - \mathrm{d}t)$, as shown in Eq. (2).

The unknown particle distribution functions at the plane boundary are expressed as a combination of the local known value and a corrector [15],

$$f_p(\vec{x}, t) = f^{*}_p(\vec{x}, t) + \frac{\alpha_p}{c}\vec{e}_p \cdot \vec{Q} \tag{8}$$

where $\vec{Q}$ is the corrector to enforce the required momentum.

Consider a typical point P_{CB} along the computational boundary shown in Fig. 2, where the unknown distribution functions are f_4, f_7 and f_8, i.e. $f_4 = f^{*}_4 - \alpha_4 Q_y, f_7 = f^{*}_7 - \alpha_7(Q_x + Q_y)$ and $f_8 = f^{*}_8 + \alpha_8(Q_x - Q_y)$. Therefore, the macroscopic velocity and density at the point P_{CB} using Eq. (3), in conjunction with Eqs. (2) and (8), can be expressed as,

$$\begin{aligned}
\rho &= f_0 + f_1 + f_2 + f_3 + (f^{*}_4 - \alpha_4 Q_y) + f_5 + f_6 + (f^{*}_7 - \alpha_7(Q_x + Q_y)) + (f^{*}_8 + \alpha_8(Q_x - Q_y)) \\
\rho u &= f_1 + f_5 + (f^{*}_8 + \alpha_8(Q_x - Q_y)) - f_3 - f_6 - (f^{*}_7 - \alpha_7(Q_x + Q_y)) \\
\rho v &= f_2 + f_5 + f_6 - (f^{*}_4 - \alpha_4 Q_y) - (f^{*}_7 - \alpha_7(Q_x + Q_y)) - (f^{*}_8 + \alpha_8(Q_x - Q_y)).
\end{aligned} \tag{9}$$

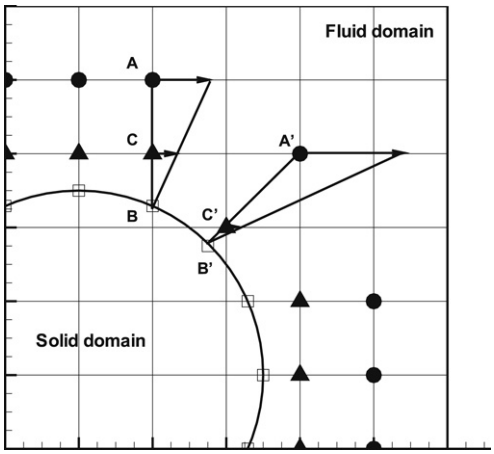

Fig. 3. Geometry of flows with an immersed boundary. ▲: correction node, □: Lagrangian marker, ●: second fluid node.

These equations can be used to solve for ρ, Q_x and Q_y, and hence f_4, f_7 and f_8. For simplicity, $\alpha_p = \omega_p$. This coefficient produces a more compact form of the distribution functions and the boundary condition of Zou and He [16] can be recovered. The explicit forms of the unknown particle distribution functions as shown below.

$$\rho = \frac{f_0 + f_1 + f_3 + 2(f_2 + f_5 + f_6)}{1 + v} \tag{10}$$

$$f_4 = f_4^* - \frac{2}{3}\rho v + \frac{2}{3}(f_2 - f_4^* + f_5 - f_7^* + f_6 - f_8^*) \tag{11}$$

$$f_7 = f_7^* - \frac{1}{2}\rho u - \frac{1}{6}\rho v + \frac{1}{2}(f_1 - f_3) + \frac{1}{6}(f_2 - f_4^*) + \frac{2}{3}(f_5 - f_7^*) - \frac{1}{3}(f_6 - f_8^*) \tag{12}$$

$$f_8 = f_8^* + \frac{1}{2}\rho u - \frac{1}{6}\rho v - \frac{1}{2}(f_1 - f_3) + \frac{1}{6}(f_2 - f_4^*) - \frac{1}{3}(f_5 - f_7^*) + \frac{2}{3}(f_6 - f_8^*). \tag{13}$$

It should be noted that, instead of deriving the explicit solution, matrix inversion of Eq. (9) is often more convenient and is normally adopted here. Also, Hou et al. [15] experimented three different f^*, i.e. $f_p^*(\vec{x}, t) = f(\vec{x}, -\vec{e}_p, t)$, $b : f_p^*(\vec{x}, t) = f(\vec{x}, \vec{e}_p, t - \mathrm{d}t)$ and $c : f_p^*(\vec{x}, t) = f^{eq}(\vec{x}, \vec{e}_p, t - \mathrm{d}t)$, and differences are observed to be negligible. This seems to suggest in the present formulation by satisfying the momentum, the influence of the choice of the local known distribution function f^* is marginal. For formulation (a), the present form recovers the form by Zou and He [16]. However, for simplicity and with lower computational effort, formulation b is adopted for the computational domain boundary.

3.2. The solid–fluid boundary technique

Here, technique employed to model the solid–fluid boundary is introduced, since the boundary does not in general coincides with the lattices. A typical solid–fluid boundary within the computational domain is shown in Fig. 2, where the closest nodes adjacent to the boundary in the fluid domain are termed the correction nodes (C) as represented by the filled triangles. The open squares are the Lagrangian markers (B) used to mimic the solid–fluid boundary, and the filled circles represent the second fluid nodes (A) beyond the correction nodes. In the present curved boundary approach, the correction nodes are used to impose the momentum condition due to the presence of the solid–fluid boundary.

The correct macroscopic velocity of the correction nodes are obtained by linear interpolation between the velocities of the Lagrangian marker (B) and the second fluid node (A), as shown in Fig. 3.

$$\vec{V}_C = \vec{V}_A + (\vec{V}_A - \vec{V}_B)\frac{\overline{AC}}{\overline{AB}}. \tag{14}$$

The determination of the location of the Lagrangian marker is addressed here. If the correction node one vertical or horizontal edge connected with the solid–fluid boundary, for example at node C, the Lagrangian marker is determined as the intersection of the line $\overrightarrow{AC}$ with the solid–fluid boundary, i.e. marker point B. However, for node C' there are one vertical and one horizontal edges connected to the solid–fluid boundary. Therefore, the interpolation is not unique. In order to avoid this ambiguity, the method proposed by Liao et al. [17] (using the Navier–Stokes solver) is adopted, that the Lagrangian marker is determined as the intersection of the line $\overrightarrow{A'C'}$ with the solid–fluid boundary, i.e. marker point B'.

As indicated earlier, LBM simulation is applied throughout the computational domain even within the solid domain, i.e. at point P_s. Therefore, after the streaming operation, distribution functions originated from the solid domain, $f_p^+(\vec{x} - \vec{e}_i\mathrm{d}t, t - \mathrm{d}t)$, will migrate to the correction nodes adjacent to the solid–fluid boundary, for example nodes C : f_2, f_5 and

C' : f_1, f_2, f_5 shown in Fig. 2. Obviously, the momentum based on these distribution functions will not be correct. Thus, measures have to be taken to modify these incorrect particle distribution functions to satisfy the momentum condition $(u_c,\ v_c)$ computed by Eq. (14).

Therefore, the particle distribution functions at these nodes are modified as,

$$f_p(\vec{x}, t) = f_p^+(\vec{x} - \vec{e}_i \mathrm{d}t, t - \mathrm{d}t) + \frac{\omega_p}{c}\vec{e}_p \cdot \vec{Q}. \tag{15}$$

Consider, for example correction node C' shown in Fig. 2, where the distribution functions needed for modification are,

$$\begin{aligned} f_1 &= f_1^+(\vec{x} - \vec{e}_1 \mathrm{d}t, t - \mathrm{d}t) + \omega_1 Q_x \\ f_2 &= f_2^+(\vec{x} - \vec{e}_2 \mathrm{d}t, t - \mathrm{d}t) + \omega_2 Q_y \\ f_5 &= f_5^+(\vec{x} - \vec{e}_5 \mathrm{d}t, t - \mathrm{d}t) + \omega_5 (Q_x + Q_y). \end{aligned} \tag{16}$$

Therefore, the macroscopic velocity and density at the point C' using Eqs. (3) and (16) can be expressed as,

$$\begin{aligned} \rho &= f_0 + f_1^+(\vec{x} - \vec{e}_1 \mathrm{d}t, t - \mathrm{d}t) + \omega_1 Q_x + f_2^+(\vec{x} - \vec{e}_2 \mathrm{d}t, t - \mathrm{d}t) + \omega_2 Q_y + f_3 + f_4 \\ &\quad + f_5^+(\vec{x} - \vec{e}_5 \mathrm{d}t, t - \mathrm{d}t) + \omega_5 (Q_x + Q_y) + f_6 + f_7 + f_8 \\ \rho u_c &= f_1^+(\vec{x} - \vec{e}_1 \mathrm{d}t, t - \mathrm{d}t) + \omega_1 Q_x + f_5^+(\vec{x} - \vec{e}_5 \mathrm{d}t, t - \mathrm{d}t) + \omega_5 (Q_x + Q_y) + f_8 - f_3 - f_6 - f_7 \\ \rho v_c &= f_2^+(\vec{x} - \vec{e}_2 \mathrm{d}t, t - \mathrm{d}t) + \omega_2 Q_y + f_5^+(\vec{x} - \vec{e}_5 \mathrm{d}t, t - \mathrm{d}t) + \omega_5 (Q_x + Q_y) + f_6 - f_4 - f_7 - f_8. \end{aligned} \tag{17}$$

It should be noted that unlike the flat boundary, the number and the direction of the incorrect distribution functions at each correction node are different along the curved boundary. Therefore, no explicit solution of Eq. (17) is derived here. Rather, matrix inversion is used to obtain density and correctors $(Q_x,\ Q_y)$, and hence f_1, f_2 and f_5. It is noted that the matrix coefficients are functions of the weighting functions of the incorrect distribution functions and are independent of the distance of the correction nodes to the wall. Similar procedure can be applied to other correction nodes to enforce the correct momentum.

4. Numerical results

4.1. Decaying vortex

In this subsection, the numerical accuracy of the Lattice Boltzmann model incorporating with the embedded boundary is examined. The test example is the decaying vortex problem which is used frequently since the analytic solution is available. The solution is shown below.

$$u(x, y, t) = -U \cos(\pi x/L) \sin(\pi y/L) \mathrm{e}^{-2\pi^2 Ut/(\mathrm{Re}L)}, \tag{18}$$

$$v(x, y, t) = U \sin(\pi x/L) \cos(\pi y/L) \mathrm{e}^{-2\pi^2 Ut/(\mathrm{Re}L)}, \tag{19}$$

$$\rho(x, y, t) = \rho_o - \frac{\rho_o U^2}{4C_s^2} [\cos(2\pi x/L) + \sin(2\pi y/L)] \mathrm{e}^{-4\pi^2 Ut/(\mathrm{Re}L)}. \tag{20}$$

In this test, the computational domain is chosen as $[-L, L] \times [-L, L]$ where $L = 1$. The dimensionless relaxation time is $\tau = 0.65$, the Reynolds number is $UL/\nu = 10$, and the computations are all up to time $Ut/L = 1$. Four different uniform grids ($N \times N, N = 41, 81, 161, 321$) are used in the simulations. The Eulerian grid spacing is $\Delta x = \Delta y = 2/(N - 1)$, the time step size is $\Delta t = \Delta x$.

The exact time varying conditions are imposed along the nodes external to the circular embedded boundary, where the radius is 0.5. The predicted velocity vector and the circular boundary are shown in Fig. 4, where the velocity vector is clearly not influenced by the presence of the circular boundary. Fig. 5 shows the maximum (or L_∞) errors for the solutions at time $Ut/L = 1$, where the errors for the Eulerian grid velocity component u are listed. The rate of convergence is computed by taking logarithmic for the ratio of the two successive errors as $Rate = \log_2 \frac{E_N}{E_{N/2}}$, where E_N denotes the error of the grid resolution N. As shown, the present method is approximately second-order accurate.

4.2. Transient flow induced by an abruptly rotating ring

Here, the flow considered is a ring rotating at the center of a square domain $[-D, D] \times [-D, D]$ where $D(= 2R)$ the diameter of the rotating ring is 1. The dimensionless relaxation time is $\tau = 0.65$ and the Reynolds number is $U_{\theta max} D/\nu = 10$. Numerical mesh adopted is 160×160. Since the ring starts abruptly from rest, the flow inside the ring is driven by the rotating ring. After the transient stage, the flow reaches solid body rotation state within the ring. The analytic solution for this rotating ring flow can be expressed as,

$$u_\theta = \sum_{n=1}^{\infty} c_n \exp\left(-\frac{\nu(\alpha_n^1)^2 t}{R^2}\right) J_1\left(\frac{\alpha_n^1 r}{R}\right) + r\Omega \tag{21}$$

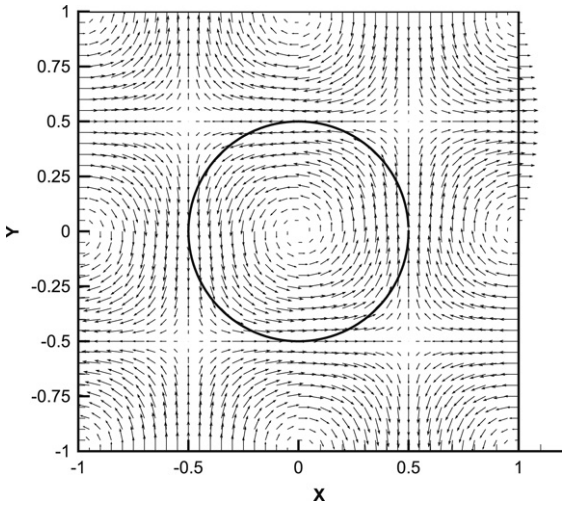

Fig. 4. Velocity vector and immersed boundary of decaying vortex.

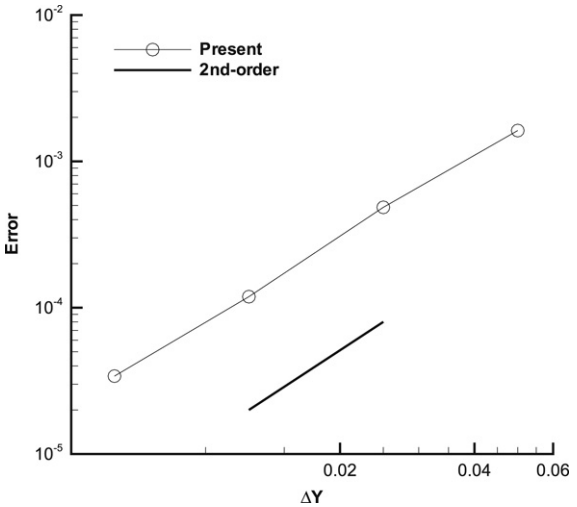

Fig. 5. Maximum relative error of decaying vortex.

where

$$c_n = \frac{\int_0^R -r^2 \Omega J_1\left(\frac{\alpha_n^1 r}{R}\right) \mathrm{d}r}{\int_0^R r J_1^2\left(\frac{\alpha_n^1 r}{R}\right) \mathrm{d}r} \tag{22}$$

$$J_1(x) = \sum_{m=0}^{\infty} \frac{(-1^m)}{m!\Gamma(m+2)} \left(\frac{x}{2}\right)^{2m+1} \tag{23}$$

α_n^1 is the n^{th} zero root of $J_1(x)$.

Numerical solutions are compared with the analytic solutions as shown in Fig. 6 at different time $t^* = \nu t/R^2$. The migration of the flow from rest to solid body rotation profiles can be clearly observed. Numerical solutions agree well with the analytic solution, indicating the accuracy of the present methodology.

4.3. Flow over an asymmetrically placed cylinder in a channel

The flow past a stationary circular cylinder is a typical problem and has been widely investigated [13,14,18,19]. For Reynolds number below 47, the flow structure remains steady with stationary recirculating vortices behind the cylinder. As the Reynolds number is elevated, the steadiness breaks down and the vortex starts to shed up and down alternatively. This shedding frequency and the intensity of the vortex also increase in tandem with the elevated level of the Reynolds number.

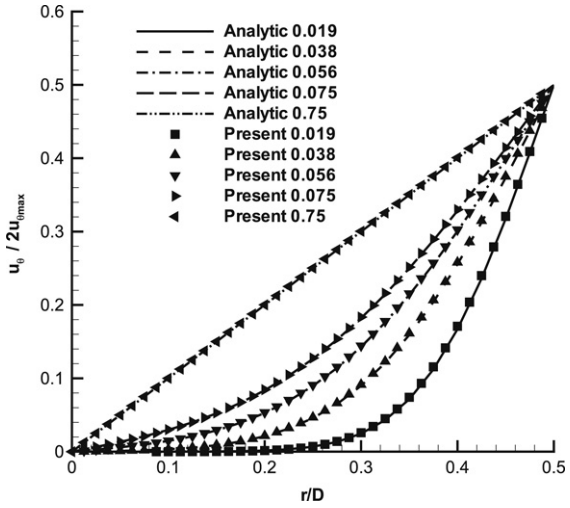

Fig. 6. The numerical velocity profiles compared with analytic resolution.

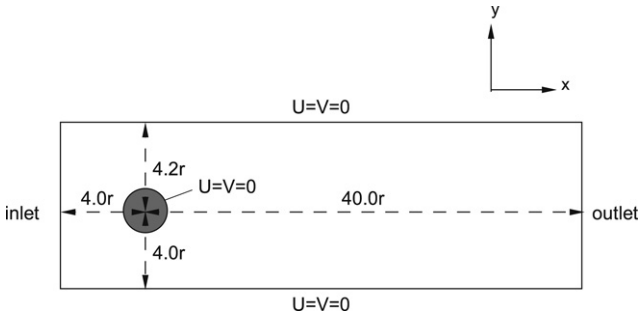

Fig. 7. Configuration of flow over an asymmetrically placed cylinder in a channel.

Schafer and Turek [18] reported a set of 2D and 3D benchmark results for laminar flows over a circular cylinder of radius r that is asymmetrically placed inside a channel. The distances from the center of the cylinder to the upper wall and lower wall are $4.2r$ and $4.0r$, respectively. The 2D geometric layout is shown in Fig. 7. The inlet boundary is placed at 4 radii upstream of the cylinder center, $l^+ = 4.0r$, and the exit boundary is located 40 radii downstream of the cylinder center. In the present study, $r = 30\Delta x$ is used. The grid resolutions in the x and y directions are 1321 and 247, respectively. The Eulerian grid spacing is $\Delta x = \Delta y = 1/40$, the time step size is $\Delta t = \Delta x$. The Reynolds numbers are $\mathrm{Re} = 2rU_{ave}/\nu = 20$ and 100. At $\mathrm{Re} = 100$, the flow becomes unsteady and periodic vortex shedding is observed.

A parabolic velocity profile of maximum speed $U_{\max}$ is applied to the inlet boundary, and the inlet Mach number of $U_{\max}$ is $Mc = U_{\max}/C_s = 0.1$. No-slip boundary condition are applied along the walls, and at the exit, linear extrapolation is applied for the unknown distribution functions.

The Reynolds number based on the average inlet velocity $U_{ave} = 2U_{\max}/3$ is $\mathrm{Re} = 2rU_{ave}/\nu$. The drag and lift coefficient over the cylinder are defined as,

$$C_D = \frac{F_D}{\rho_{in} U_{ave}^2 r}, \qquad C_L = \frac{F_L}{\rho_{in} U_{ave}^2 r}. \tag{24}$$

The drag force (F_D) and lift force (F_L) generated by the cylinder can be obtained by integrating the local pressure and stress distributions along the cylinder wall. However, this method may not be straightforward due to the interpolation procedure involved. Another simple alternative is by applying the volume integral of the Navier–Stokes equation, and the momentum deficits due to the presence of the cylinder are the drag and lift, i.e.

$$\begin{aligned} -F_D &= \int_{vol} \left(\frac{\partial \rho u}{\partial t} + \frac{\partial \rho uu}{\partial x} + \frac{\partial \rho uv}{\partial y} + \frac{\partial p}{\partial x} - \nu \left[\frac{\partial}{\partial x} \left(2\rho \frac{\partial u}{\partial x} \right) + \frac{\partial}{\partial y} \rho \left(\frac{\partial v}{\partial x} + \frac{\partial u}{\partial y} \right) \right] \right) \mathrm{d}vol \\ -F_L &= \int_{vol} \left(\frac{\partial \rho v}{\partial t} + \frac{\partial \rho uv}{\partial x} + \frac{\partial \rho vv}{\partial y} - \nu \left[\frac{\partial}{\partial x} \rho \left(\frac{\partial v}{\partial x} + \frac{\partial u}{\partial y} \right) + \frac{\partial}{\partial y} \left(2\rho \frac{\partial v}{\partial y} \right) \right] \right) \mathrm{d}vol. \end{aligned} \tag{25}$$

Here, the divergence of the velocity field is small and is neglected.

Table 1
C_D variations using different grid for the flow over a cylinder asymmetrically placed in a channel at Re = 20.

GRID	C_D Eq. (25)	C_D Eq. (26)	$C_D - C_{Dref}$ Eq. (26)	Order
440 × 82	5.637127	5.637792	0.030657	
880 × 164	5.614934	5.614887	0.007752	1.99
1320 × 246 (ref)	5.607235	5.607135	0	

Table 2
C_D and C_L for the flow over a cylinder asymmetrically placed in a channel at Re = 20.

Re = 20	Present method	Chen et al. [14]	Schäfer and Turek [18]
C_D	5.607	5.679	5.57–5.59
C_L	0.0113	0.0114	0.0104–0.0110

Table 3
C_D, C_L, and St for the flow over a cylinder asymmetrically placed in a channel at Re = 100.

Re = 100	Present method	Chen et al. [14]	Mei et al. [19]	Schäfer and Turek [18]
C_D	3.292	3.333	3.2275	3.22–3.24
C_L	0.974	1.0511	1.0040	0.99–1.01
St	0.302	0.3003	0.3033	0.295–0.305

In the present study, another alternative to compute the drag and lift incurred by the presence of the cylinder is proposed here. It should be noted that in the present curved boundary technique, there is no force applied at the correction nodes. Therefore, a measure must be adopted to evaluate the force. By assuming that a fictitious force exists at each correction node to produce momentum change in the process of velocity modification, for example Eq. (16), thus the force is evaluated as,

$$\begin{aligned}\Delta t\vec{F} &= \sum_p f_p\vec{e}_p + \sum_{i\neq p} f_i\vec{e}_i - \left[\sum_p f_p^+(\vec{x} - \vec{e}_i\mathrm{d}t, t - \mathrm{d}t)\vec{e}_p + \sum_{i\neq p} f_i\vec{e}_i\right] \\ &= \sum_p \frac{\omega_p}{c}[\vec{e}_p \cdot \vec{Q}]\vec{e}_p \end{aligned} \tag{26}$$

where p is the incorrect distribution function at the correction node and is defined in Eq. (15).

Thus the drag force F_D and the lift force F_L are obtained from the following equations [13],

$$F_D = -\sum_m F_{x,m}\Delta x^2, \qquad F_L = -\sum_m F_{y,m}\Delta x^2 \tag{27}$$

where m represents the correction node adjacent to the cylinder boundary. Once this fictitious force is obtained, the drag and lift coefficient is easily determined by Eqs. (24) and (27).

Flows at Re = 20 and Re = 100 are simulated. The flow is steady when the Reynolds number is equal to 20. Table 1 shows the influences of the lattice sizes and force computing methods on the predicted drag coefficient at Re = 20. It is clear that the proposed method agrees perfectly with the volume integral method and the present method is second order accurate. Similar trend is observed for the lift coefficient. The predicted drag and lift coefficient remain constant after sufficient time steps, and compares favorably with other solutions as shown in Table 2.

At Re = 100, periodic vortex shedding is observed. The drag and lift coefficient have a periodic fluctuation, as shown in Figs. 8 and 9. Two peaks in the drag coefficients correspond to the existence of a weaker vortex and a stronger vortex alternately shed behind the cylinder. This phenomenon is due to the cylinder is asymmetrically placed in the channel. Instantaneous vorticity contour at Re = 100 is shown in Fig. 10. Table 3 lists the maximum of C_D, C_L and the Strouhal number of the simulation. The present results are shown to be compatible with previous numerical methods. The predicted Strouhal number $St = 2r/U_{ave}T$ is 0.3002. This agrees very well with the range of Strouhal number (0.2950-0.3050) given in Ref. [18].

5. Conclusion

In this paper, the boundary condition proposed by Hou et al. [15] is extended to simulate flows embedded with complex solid object. Present LBM simulation is applied throughout the computational domain even within the solid object. Therefore, two different boundary conditions are addressed. The boundary condition along the flat computational domain, where the boundary coincides with the lattice, is similar to that proposed by Hou et al. [15]. A novel technique is used to model the existence of the solid–fluid boundary. The solid–fluid boundary is represented by a series of Lagrangian markers and the closest nodes adjacent to the boundary in the fluid domain are used as boundary nodes of the flow domain. The fluid velocity of the boundary node is obtained by linear interpolation between the velocities of the Lagrangian marker

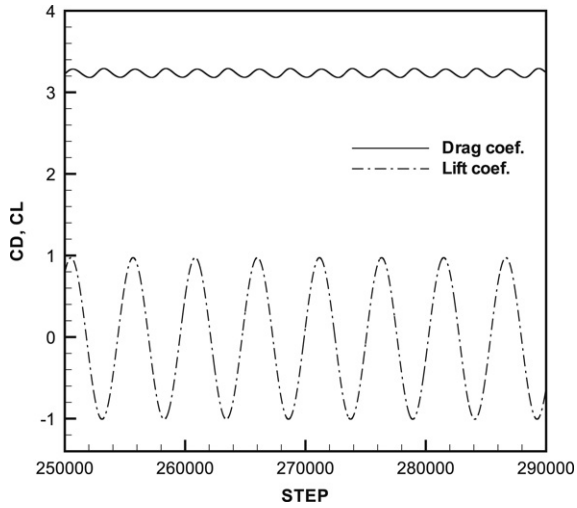

Fig. 8. The time evolution of drag and lift coefficients at Re = 100.

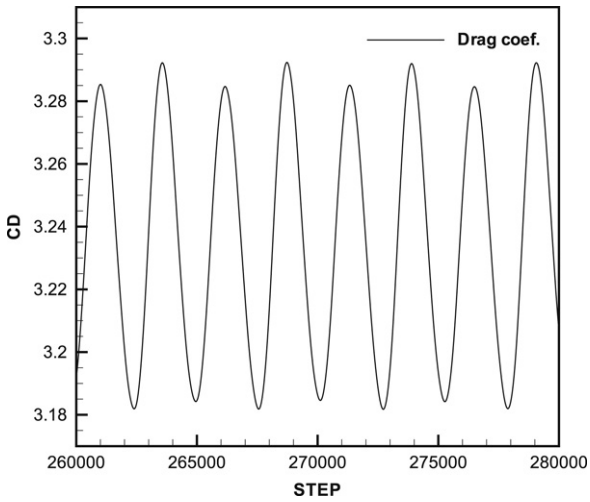

Fig. 9. The time evolution of drag coefficients at Re = 100.

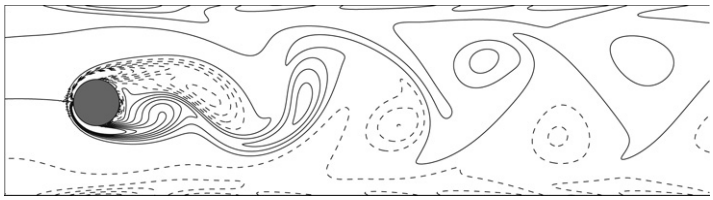

Fig. 10. The instantaneous vorticity contours at Re = 100, dotted and solid lines denote negative and positive contours.

and the second fluid node further away. Then the distribution functions originates from the solid domain at the boundary nodes are modified using known distribution functions and correctors to satisfy the momentum. The technique is examined by simulating decaying vortex, transient flow induced by an abruptly rotating ring and flow over an asymmetrically placed cylinder. Numerical simulations indicate that this method is second order accurate. A fictitious force formulation is proposed to compute the drag and lift forces for flows over asymmetrically placed cylinder and the predicted forces agree perfectly with the more elaborate integral method. The predicted drag and lift coefficient are compatible with the benchmark solutions, indicating the capability of the present method.

Acknowledgments

The authors gratefully acknowledge the support by the Taiwan National Science Council (grant 94-2212-E-007-059) and the computational facilities provided by the Taiwan National Center for High-Performance Computing.

References

[1] S. Chen, H. Chen, D.O. Martinez, W.H. Matthaeus, Lattice Boltzmann model for simulation of magnetohydrodynamics, Phys. Rev. Lett. 67 (1991) 3776.
[2] Y.H. Qian, D. d'Humières, P. Lallemand, Lattice BGK model for Navier–Stokes equation, Europhys. Lett. 17 (1992) 479.
[3] S. Chen, G.D. Doolen, Lattice Boltzmann method for fluid flow, Annu. Rev. Fluid Mech. 30 (1998) 329.
[4] S. Chen, D.O. Martinez, R. Mei, On boundary conditions in lattice Boltzmann methods, Phys. Fluids 8 (1996) 2527.
[5] O. Filippova, D. Hänel, Grid refinement for lattice-BGK models, J. Comput. Phys 147 (1998) 219.
[6] R. Mei, L.S. Luo, W. Shyy, An accurate curved boundary treatment in the lattice Boltzmann method, J. Comput. Phys 155 (1999) 307.
[7] P. Lallemand, L.S. Luo, Lattice Boltzmann method for moving boundaries, J. Comput. Phys. 184 (2003) 406.
[8] M. Bouzidi, M. Firdaouss, P. Lallemand, Momentum transfer of a Boltzmann-lattice fluid with boundaries, Phys. Fluids **1**3 (2001) 3452.
[9] M. Junk, Z.X. Yang, One point boundary condition for the lattice Boltzmann method, Phys. Rev. E 72 (Part 2) (2005) 066701.
[10] C.S. Peskin, Flow patterns around heart valves: A numerical method, J. Comput. Phys. 10 (1972) 252.
[11] E.M. Saiki, S. Biringen, Numerical simulation of a cylinder in uniform flow: Application of a virtual boundary method, J. Comput. Phys. 123 (1996) 450.
[12] E.A. Fadlun, R. Verzicco, P. Orlandi, J. Mohd-Yusof, Combined immersed-boundary finite-difference methods for three-dimensional complex flow simulations, J. Comput. Phys. 161 (2000) 30.
[13] S.W. Su, M.C. Lai, C.A. Lin, An immersed boundary technique for simulating complex flows with rigid boundary, Comput. & Fluids **3**6 (2007) 313.
[14] D.J. Chen, K.H. Lin, C.A. Lin, Immersed boundary method based lattice Boltzmann method to simulate 2D and 3D complex geometry flows, Internat. J. Modern Phys. C 18 (2007) 585.
[15] C.F. Hou, C. Chang, C.A. Lin, Consistent boundary conditions for 2D and 3D Lattice Boltzmann simulations (submitted for publication).
[16] Q. Zou, X. He, On pressure and velocity boundary conditions for the lattice Boltzmann BGK model, Phys. Fluids 9 (1997) 1591.
[17] C.C. Liao, Y.W. Chang, C.A. Lin, J.M. McDonough, Simulating flows with moving rigid boundary using immersed boundary method (submitted for publication).
[18] M. Schafer, S. Turek, in: E.H. Hirschel (Ed.), Flow Simulation with High-Performance Computer II, in: Notes in Numerical Fluid Mechanics (Vieweg, Braunschweig), vol. 52, 1996, p. 547.
[19] R. Mei, D. Yu, W. Shyy, L.S. Luo, Force evaluation in the lattice Boltzmann method involving curved geometry, Phy. Rev. E 65 (2002) 041203.